The HWRF Hurricane Ensemble Data Assimilation System (HEDAS) for High-Resolution Data: The Impact of Airborne Doppler Radar Observations in an OSSE

ALTUĞ AKSOY AND SYLVIE LORSOLO

Cooperative Institute for Marine and Atmospheric Studies, University of Miami, and Hurricane Research Division, NOAA/AOML, Miami, Florida

TOMISLAVA VUKICEVIC

Hurricane Research Division, NOAA/AOML, Miami, Florida

KATHRYN J. SELLWOOD

Cooperative Institute for Marine and Atmospheric Studies, University of Miami, and Hurricane Research Division, NOAA/AOML, Miami, Florida

SIM D. ABERSON

Hurricane Research Division, NOAA/AOML, Miami, Florida

FUQING ZHANG

Department of Meteorology, The Pennsylvania State University, University Park, Pennsylvania

(Manuscript received 10 August 2011, in final form 6 December 2011)

ABSTRACT

Within the National Oceanic and Atmospheric Administration, the Hurricane Research Division of the Atlantic Oceanographic and Meteorological Laboratory has developed the Hurricane Weather Research and Forecasting (HWRF) Ensemble Data Assimilation System (HEDAS) to assimilate hurricane inner-core observations for high-resolution vortex initialization. HEDAS is based on a serial implementation of the square root ensemble Kalman filter. HWRF is configured with a horizontal grid spacing of 9/3 km on the outer/inner domains. In this preliminary study, airborne Doppler radar radial wind observations are simulated from a higher-resolution (4.5/1.5 km) version of the same model with other modifications that resulted in appreciable model error.

A 24-h nature run simulation of Hurricane Paloma was initialized at 1200 UTC 7 November 2008 and produced a realistic, category-2-strength hurricane vortex. The impact of assimilating Doppler wind observations is assessed in observation space as well as in model space. It is observed that while the assimilation of Doppler wind observations results in significant improvements in the overall vortex structure, a general bias in the average error statistics persists because of the underestimation of overall intensity. A general deficiency in ensemble spread is also evident. While covariance inflation/relaxation and observation thinning result in improved ensemble spread, these do not translate into improvements in overall error statistics. These results strongly suggest a need to include in the ensemble a representation of forecast error growth from other sources such as model error.

Corresponding author address: Dr. Altuğ Aksoy, CIMAS, Rosenstiel School, 4600 Rickenbacker Cswy., Miami, FL 33149.
E-mail: aaksoy@rsmas.miami.edu

DOI: 10.1175/MWR-D-11-00212.1

1. Introduction

In recent years, there has been a marked improvement in our ability to predict hurricane tracks, while forecasting intensity has remained a major challenge with virtually no improvement in this area (e.g., Berg and Avila 2011). A recent study by Kaplan et al. (2010) found that large-scale atmospheric factors outside the hurricane core (e.g., vertical wind shear, upper-level divergence, and low-level moisture) are only able to capture 35%–65% of the skill in predicting rapid intensification (RI) for a 25-kt threshold (see their Fig. 17c). This result suggests that further skill may be obtained by factors associated with the inner-core vortex dynamics and the upper ocean.

While operational regional hurricane forecast models like the Hurricane Weather Research and Forecasting (HWRF) model (e.g., Rappaport et al. 2009) and the Geophysical Fluid Dynamics Laboratory (GFDL) Hurricane Prediction System (e.g., Bender et al. 2007) are initialized with mostly model-derived, nearly axisymmetric vortices, recent research is beginning to convincingly point to the importance of asymmetric vortex structure in determining storm evolution (e.g., Reasor et al. 2004; Mallen et al. 2005; Nguyen et al. 2008; Rogers 2010). Consequently, better initial vortices that are consistent with the observed internal dynamics may be necessary for successful hurricane intensity forecasts (e.g., Houze et al. 2007; Chen et al. 2007). This could be created with advanced data assimilation techniques.

In the past two decades, two categories of state-of-the-art data assimilation techniques have evolved: variational and ensemble based (e.g., Kalnay 2003). In the specific area of high-resolution hurricane data assimilation, more focus has been so far given to variational techniques (e.g., Zhao and Jin 2008; Xiao et al. 2007; Pu et al. 2009; Xiao et al. 2009). While the positive impact of data assimilation on hurricane intensity forecasts is demonstrated in these studies, success was limited because of the limitation of the variational methods in utilizing a background error covariance matrix with spatial and cross correlations characteristic of the underlying vortex flow. As an alternative, the ensemble Kalman filter (EnKF) utilizes an ensemble of short-range forecasts to estimate flow-dependent spatial and cross correlations for data assimilation (Evensen 1994; Houtekamer and Mitchell 1998). Recent success with assimilating radar observations of continental convective storms (e.g., Snyder and Zhang 2003; Zhang et al. 2004; Dowell et al. 2004, 2011; Aksoy et al. 2009, 2010) has raised hopes that high-resolution hurricane models, too, can benefit from the EnKF. In a proof-of-concept study, Zhang et al. (2009) demonstrated that the EnKF exhibited more skill than three-dimensional variational data assimilation (3DVAR) in predicting the rapid formation and intensification of a landfalling hurricane using observations from a land-based radar. The same data assimilation system was then recently tested with airborne Doppler radar observations (Weng and Zhang 2012; F. Zhang et al. 2011) and demonstrated improvement in the representation of the vortex structure in Hurricane Katrina (2005), as well as reduction in intensity forecast error in 61 cases from 2008 to 2010 when compared to operational dynamical models. In this paper, assimilation experiments with simulated airborne Doppler radar data using an EnKF are conducted to focus on how the assimilation of Doppler radar data impacts the high-resolution representation of the hurricane vortex.

The National Oceanic and Atmospheric Administration (NOAA) has been collecting high-resolution airborne observations in hurricanes for over 30 yr using NOAA's WP-3D (P-3) aircraft (e.g., Aberson et al. 2006), and for 15 yr from NOAA's high-altitude Gulfstream-IV jet (e.g., Aberson 2010). Recently, the Hurricane Research Division (HRD) at the Atlantic Oceanographic and Meteorological Laboratory (AOML) has built a high-resolution, ensemble-based data assimilation system to utilize these observations [Hurricane Ensemble Data Assimilation System (HEDAS)]. HEDAS comprises an EnKF and HRD's experimental HWRF model (Gopalakrishnan et al. 2011).

The current article focuses on the assimilation of *simulated* airborne Doppler radar observations using HEDAS. The purpose is to demonstrate how this data assimilation approach produces hurricane vortex analyses in a controlled environment through observing system simulation experiments (OSSEs). A realistic nature run provides the "truth" from which radar observations are extracted. Having full three-dimensional fields available from a nature run further facilitates an in-depth analysis of the performance of HEDAS based on a multitude of criteria relevant to hurricane structure and dynamics that otherwise would not be possible with real data. The availability of such a nature run will allow for impact studies of various observation types as well as developing alternative observation processing methodologies. Subsequent papers will also focus on results with real data.

The experimental setup, along with the details of the data assimilation and modeling systems, is described in section 2. Section 3 details the simulation of the flight track and observations, while section 4 presents a description and quantitative evaluation of the nature run. Section 5 continues with the presentation of HEDAS data assimilation results; the summary and discussion are in section 6.

2. Experimental setup

a. HRD's experimental HWRF

A detailed comparison between HRD's experimental HWRF and operational HWRF (e.g., Rappaport et al.

2009) can be found in Gopalakrishnan et al. (2011). Most of the differences between operational HWRF and HRD's experimental HWRF arise from the choice of physical parameterization schemes and resolution. For example, operational HWRF has a nominal horizontal grid spacing of 27/9 km for the outer/inner domains, while experimental HWRF horizontal grid spacing is 9/3 km. In the current study, the vortex-following nest motion of the inner domain (Gopalakrishnan et al. 2002, 2006), a feature in both the experimental and operational versions of HWRF, is suppressed during the spinup and data assimilation cycles. This allows all ensemble members to be initialized with collocated inner domains to facilitate gridpoint-based spatial covariance computations in the EnKF.

b. HEDAS

HEDAS employs the EnKF, which uses an ensemble of short-range forecasts to estimate background error covariances of the model state. The prior joint sample covariances obtained from the ensemble are used to linearly regress observation innovations (differences between observations and model forecasts in observation space) to obtain prior state vector increments. The update loop that processes model grid points within the influence region is parallelized using Open Multi-Processing (OpenMP) architecture. While OpenMP implementations are limited to the respective number of computing cores on a given processor, they offer the advantages of memory sharing, thereby reducing the number of communications among parallel threads (Chapman et al. 2007).

Similar to Zhang et al. (2009), HEDAS is based on a serial implementation of the square root EnKF of Whitaker and Hamill (2002). In a serial update loop, each observation is treated as a scalar quantity, and the update equations of Whitaker and Hamill (2002) are simplified following Eqs. (4)–(7) in Snyder and Zhang (2003). The square root EnKF is designed to eliminate the need to perturb observations, which is shown to increase the sampling error and thus reduce the accuracy of the analysis-error covariance estimate (Whitaker and Hamill 2002).

Three-dimensional, distance-dependent covariance localization, using a compactly supported fifth-order correlation function following Gaspari and Cohn (1999), is applied. The horizontal localization length scale is chosen to be 80 grid points (~240 km) so that most of the vortex is updated given the limited spatial distribution of observations in each cycle [see discussion in section 4b (point i); Fig. 8a]. In addition, state–space inflation (Hamill and Whitaker 2005) and covariance relaxation (Zhang et al. 2004) techniques are available to counteract the underestimation of variance.

In HEDAS, data assimilation is only performed in the inner domain, to focus on the impact of high-resolution aircraft data on vortex-scale dynamics. To minimize discontinuities along the boundaries between the domains with and without data assimilation, a buffer zone is created within the inner domain along the boundaries where the impact of data assimilation is gradually reduced to zero following a distance-dependent weighting function similar to the fifth-order correlation function in Gaspari and Cohn (1999).

In the current application, HEDAS uses 30 ensemble members. The initial ensemble perturbations are obtained from operational National Centers for Environmental Prediction (NCEP) Global Ensemble Forecast System (GENS) analyses. A 6-h ensemble spinup run is carried out to develop appropriate covariance structures relevant for the scales at which the data assimilation is performed. To simulate an actual P-3 flight, 4 h of observations are divided into 48-min intervals. A final vortex analysis is obtained by the end of this period. The general schematic of the experimental setup is depicted in Fig. 1.

The types of observations currently assimilated in HEDAS include Doppler radial wind, dropwindsonde/flight-level wind, temperature, and specific humidity, and Stepped Frequency Microwave Radiometer (SFMR) 10-m equivalent wind speed, although the focus of the current study is on Doppler wind observations only. Updated model fields include zonal wind speed (u), meridional wind speed (v), sensible temperature (T), specific humidity (q), total cloud water mixing ratio (c_{wm}), and hydrostatic pressure (p_d). The HEDAS configuration is summarized in Table 1.

c. Description of data assimilation experiments

To test how the data assimilation system performs and to determine an optimal filter configuration for data assimilation, several experiments are conducted (Table 1): In the control (CTRL) experiment, no data assimilation is performed. In DA_BASIC, data assimilation is carried out using a realistic volume of observations with no special treatment of ensemble variance (i.e., no covariance inflation or covariance relaxation). As ensembles are commonly known to be spread deficient in limited-area ensemble-based data assimilation (Meng and Zhang 2011), various experiments are performed to investigate the potential impacts of covariance inflation and observation thinning on ensemble spread. In DA_INF, DA_BASIC is repeated with a combination of 5% covariance inflation and 75% covariance relaxation to potentially counter insufficient ensemble spread due to sampling and/or model error. These values are commonly used in

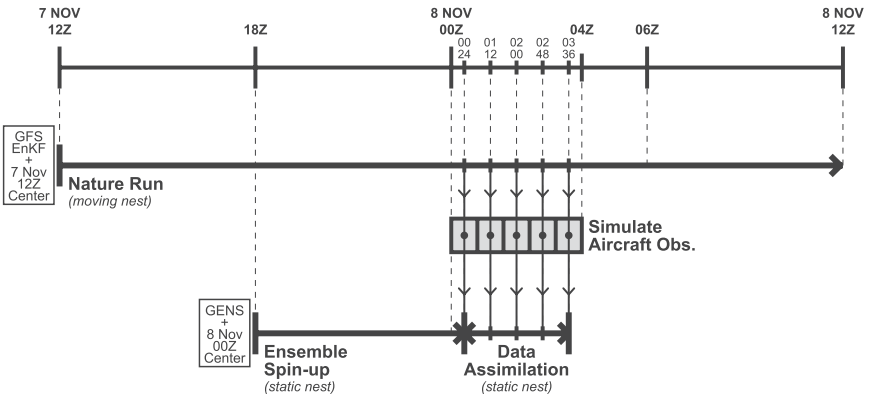

FIG. 1. General schematic of the experimental setup.

other data assimilation systems (Meng and Zhang 2011). Finally, in DA_25%OBS, one-quarter of the volume of observations used in DA_INF is randomly selected and assimilated in each assimilation cycle to investigate the potential impact of data volume on analyses. (Combinations with varying values of inflation parameters and thinning ratios are also tested but did not produce qualitatively different results.)

3. Simulation of the flight track and airborne Doppler wind observations

In the current study, a standard butterfly-type flight pattern (Fig. 2) that follows storm motion is simulated. Similar to a typical NOAA P-3 hurricane flight, the aircraft altitude is 3000 m, with an assumed ground speed of 115 m s^{-1}. The total flight duration is assumed

TABLE 1. Summary of experimental setup.

Feature	Explanation
HEDAS	
Filter type	Ensemble square root filter
Ensemble size, initialization	30 members, initialized from GFS analysis ensemble, 6-h spinup
Covariance localization, radii of influence	Through a compactly supported fifth-order correlation function, 80 grid distances in the horizontal and 15 model levels in the vertical
Assimilation domain	Static inner nest during spinup and assimilation, 3-km horizontal resolution, with a 10–gridpoint ''buffer zone'' to outer nest
Assimilation period, frequency	4 h, 48 min
Assimilated observation types	Simulated airborne Doppler radial velocity superobservations
Observation error (std dev)	
Doppler wind	11.2 m s^{-1} (uncorrelated)
Experimental HWRF	
Model version	WRF Nonhydrostatic Mesoscale Model (NMM) core, version 3.0.1.1
Resolution	Horizontal: 9-km outer nest of approximate size 60° × 60°, 3-km inner nest of approximate size 6° × 6°; vertical: 42 eta levels with model top at 50 hPa
Physics	Ferrier et al. (2002): microphysics, Hong and Pan (1998): cumulus (only in the outer domain; explicit convection in the inner domain), Dudhia (1989): shortwave radiation, Mlawer et al. (1997): longwave radiation, Hong and Pan (1996): PBL, Moon et al. (2007): surface layer, and Ek et al. (2003): land surface parameterization
Nature run	
Resolution	Horizontal: 4.5-km outer, 1.5-km vortex-following inner nests; vertical: 42 eta levels
Initial and boundary conditions	From experimental GFS/EnKF analyses and forecasts
Physics	Same as in data assimilation, except with explicit convection in both domains
Data assimilation experiments	
CTRL	No data assimilation (control)
DA_BASIC	HEDAS with no covariance inflation/relaxation
DA_INF	DA_BASIC with 5% covariance inflation, 75% covariance relaxation
DA_25%OBS	DA_INF with 25% of the volume of observations

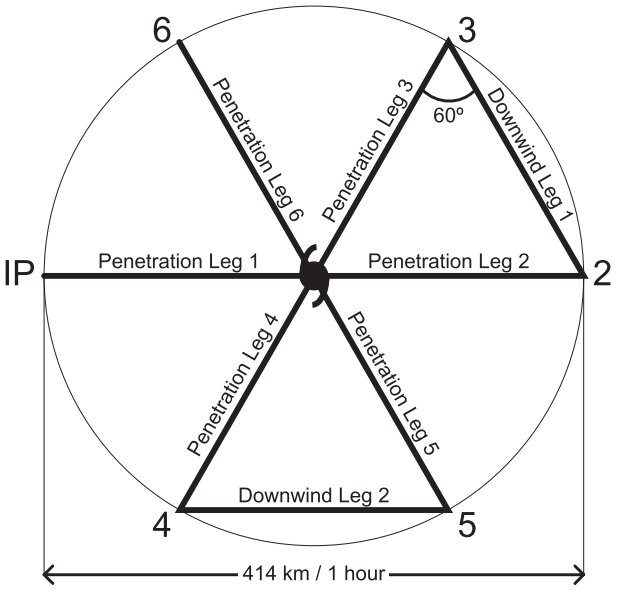

FIG. 2. General schematic of the simulated butterfly flight pattern in a storm-relative framework. In practice, any orientation of the flight pattern may be flown, to permit the location of the initial point (IP) and final point to be closest to the base of operations. In the current implementation, the IP is simulated to be due west.

to be 4 h and the storm-relative length of the radial legs is 207 km.

For the simulation of Doppler radial velocities, the plane attitude parameters (pitch, roll, drift) are assumed to be zero for simplicity and a unique track angle is assigned for each pass. At each geographical position of the radar along the flight track, radar rays are simulated in accordance with the fore–aft scanning strategy (Gamache et al. 1995). Then, for each ray, the associated azimuth and tilt angles are converted from aircraft-relative to earth-relative values.

Radar bins along each ray are simulated using the nominal NOAA P-3 tail radar gate-to-gate resolution (150 m), and individual bin positions along a ray are retrieved from the latitude and longitude of the radar, the azimuth and elevation of the ray, and the distance from the radar. Then, wind components predicted in the nature run are interpolated to each radar bin position and the Doppler radial speed is computed using the forward operator given by

$$v_r = (\sin\alpha \cos\varphi_e)u + (\cos\alpha \cos\varphi_e)v + (\sin\varphi_e)w. \quad (1)$$

Here, u, v, and w refer to model-predicted zonal, meridional, and vertical wind speed, respectively, and α and φ_e are earth-relative azimuth and elevation angles of the radar beam, respectively. The projection involved in v_r assumes that the incoming data are corrected for terminal fall speed (e.g., Black et al. 1996) so that they reflect the true vertical wind speed along the radar beam.

To obtain realistic simulated Doppler radial observations, a threshold on the cloud water content (7.5×10^{-5} g kg^{-1}) is prescribed, and this is used as a proxy to limit data when too few scatterers exist to produce reasonable radar echoes. (This parameter value is chosen subjectively from among several values tested, based on the spatial distribution of Doppler radial wind observations it produced.) In addition, radar rays are limited to 75 km in range from the radar. (This corresponds to the unambiguous maximum range dictated by the pulse repetition frequency used in real-time NOAA P-3 operations in hurricane conditions.) Finally, additive random noise (2 m s^{-1}) is applied to simulate instrument error. Observation errors are assumed to be uncorrelated, so that only the diagonal part of the observation error covariance matrix is simulated.

Because the radar spatial resolution is greater than the model resolution, which can result in large amounts of potentially correlated data, the simulated Doppler data are subsampled at 3-km resolution by ''superobbing.'' The superobbing method employed here is essentially data averaging intended for real-time data assimilation as described in Zhang et al. (2009).

4. The nature run

a. Case description: Hurricane Paloma (2008)

This study uses a case from Hurricane Paloma (2008). The goal here is not to obtain a faithful reproduction of Hurricane Paloma in a nature run, but to use a model representation of the observed storm as a reference to initialize from. This is done to ensure that there is a realistic hurricane vortex present in the nature run simulation from which inner-core observations are simulated. The nature run, therefore, serves only as a hypothetical but realistic truth to compare data assimilation results to. Consequently, this study does not compare the details of the vortex evolution in the nature run to the observed storm structure.

The life cycle of Hurricane Paloma (2008) is documented in detail in the National Hurricane Center's (NHC) tropical cyclone report on Hurricane Paloma (Brown et al. 2010). The storm reached hurricane status at 0000 UTC 7 November and subsequently underwent RI when its intensity increased by 50 kt (1 kt = 0.5144 m s^{-1}) in 24 h starting at 1200 UTC 7 November. The 24-h nature run simulation overlaps with the observed RI period. The nature run simulation, too, undergoes intensification during the same period, although not as rapidly as in reality in part because of initialization from a broad and weak initial vortex from a low-resolution global model.

b. Model description

Many aspects of the experimental HWRF model are modified from its HEDAS configuration to avoid an identical-twin scenario where a lack of model error could potentially impede the realism of an OSSE (Atlas 1997). The following modifications are introduced to obtain a realistic nature run with sufficient model differences to amount to reasonable model error:

(i) The nature run horizontal grid spacing is half of that used in HEDAS (4.5/1.5 km).
(ii) Initial and boundary conditions are obtained from the experimental Global Forecast System (GFS)/EnKF ensemble (Hamill et al. 2011), a higher-resolution (T382L64) global data assimilation and forecasting system than the GENS that initializes the HEDAS ensemble. A single GFS/EnKF ensemble member that had the best 18-h forecast of storm central pressure and location valid at 0600 UTC 8 November is chosen to initialize the OSSE run.
(iii) The nature run uses explicit convection in both domains (cf. HEDAS configuration in Table 1).
(iv) The nature run is initialized 6 h earlier than the initialization of the HEDAS ensemble.
(v) In the nature run, a vortex-following inner domain is implemented, whereas in HEDAS, the inner domain in ensemble members is static.

In the current application, the duration of the nature run simulation is 24 h, short enough to ensure that the nature run and the background HEDAS ensemble are not too divergent from each other at the onset of data assimilation. Such a scenario would likely significantly violate the linearity and ''Gaussianity'' assumptions of the EnKF.

c. Quantitative evaluation of the nature run

The storm produced within the nature run is analyzed to establish an overall framework of reference with which to compare data assimilation results presented later. All the time series discussed here are from 12-min-resolution model output, processed using a 1-h low-pass filter to remove high-frequency variability.

1) Storm track and intensity

The storm track in the nature run (Fig. 3) is generally toward the northeast but meanders in the first 6 h of simulation (likely due to the initial adjustment process resulting from an imbalance between the initial vortex from the low-resolution global model and model dynamics at 1.5-km horizontal resolution). Minimum sea level pressure (MSLP; Fig. 4a) decreases steadily from 997 to 974 hPa. Meanwhile, large fluctuations in maximum 10-m wind speed (V10max; Fig. 4a) are observed throughout the simulation. Storm intensity generally increases from an initial tropical storm (~25 m s^{-1}) to a category-2 hurricane (~40 m s^{-1}).

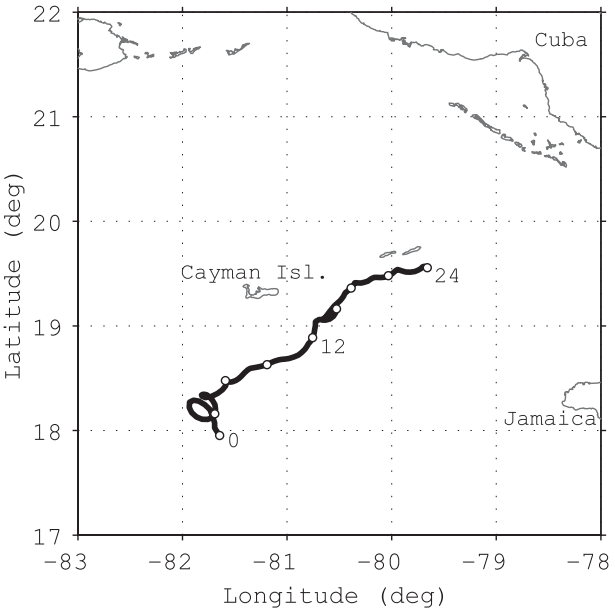

FIG. 3. Storm track in the nature run simulation. Track position is measured by the MSLP and is plotted every 12 min. Position circles are plotted every 3 h.

Since V10max is frequently tied to small-scale features of the vortex flow, we also investigate more robust and dynamically relevant fields of the vortex in the nature run simulation to obtain a general understanding of intensity evolution. Two such fields are the maximum azimuthally averaged tangential and radial components of the horizontal wind (VT and VR, respectively). The evolution of the overall maxima of these fields is shown in Fig. 4a. Both metrics indicate a steadier intensification than V10max and point to a gradual spinup of the primary and secondary circulations. (Note that the maximum azimuthally averaged tangential wind speed usually occurs higher in the boundary layer and can, therefore, be greater in magnitude than V10max, as observed between 12 and 21 h of the simulation.)

Finally, maximum updraft speed (Wmax), which characterizes the intensity of convection within the vortex, is computed. Figure 4b shows that Wmax exceeding 10 m s^{-1} quickly develops in the simulation within 2 h. Wmax then remains mostly steady at around 12 m s^{-1}.

2) Kinematic structure

The vortex structure in the nature run simulation is analyzed through time series of various quantities (Fig. 5).

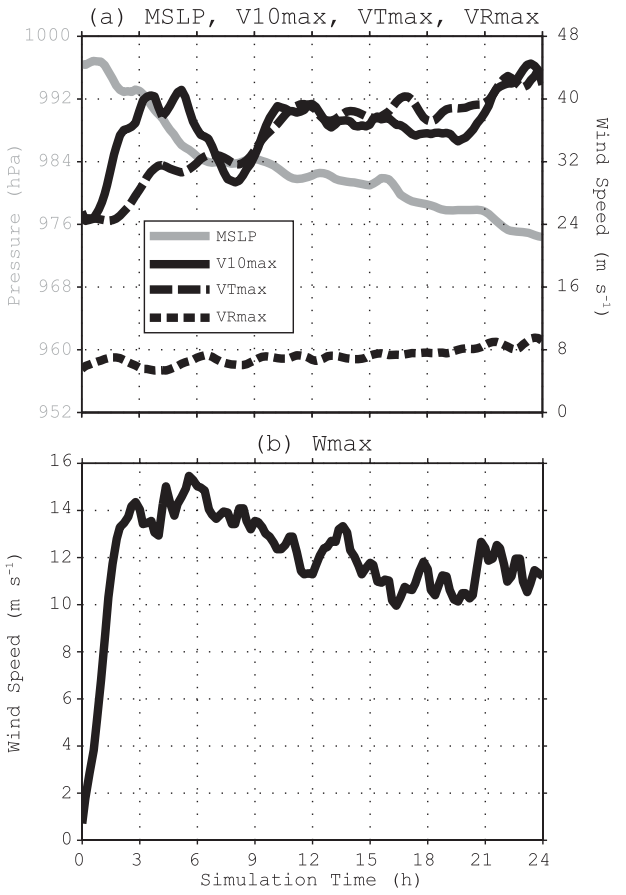

FIG. 4. Diagnostics of intensity for the nature run simulation. (a) MSLP (solid gray line; scale plotted on the left *y* axis), V10max (solid black line; scale plotted on the right *y* axis), VTmax (dashed black line; scale plotted on the right *y* axis), and VRmax (dotted black line; scale plotted on the right *y* axis). (b) Maximum updraft speed.

Radial aspects of the azimuthally averaged vortex are shown in Fig. 5a. The radius of maximum azimuthally averaged VT (radius of maximum wind; RMW)[1] exhibits a gradual decrease from 80 to about 40 km. The maximum radius of hurricane-force, 10-m wind speed (Rad_Hur) generally follows RMW evolution with slightly greater magnitude, meaning that hurricane-force winds extend to just outside RMW during most of the simulation. Meanwhile, the maximum radius of tropical-storm-force, 10-m wind speed (Rad_TS) exhibits much larger fluctuations throughout the entire simulation period.

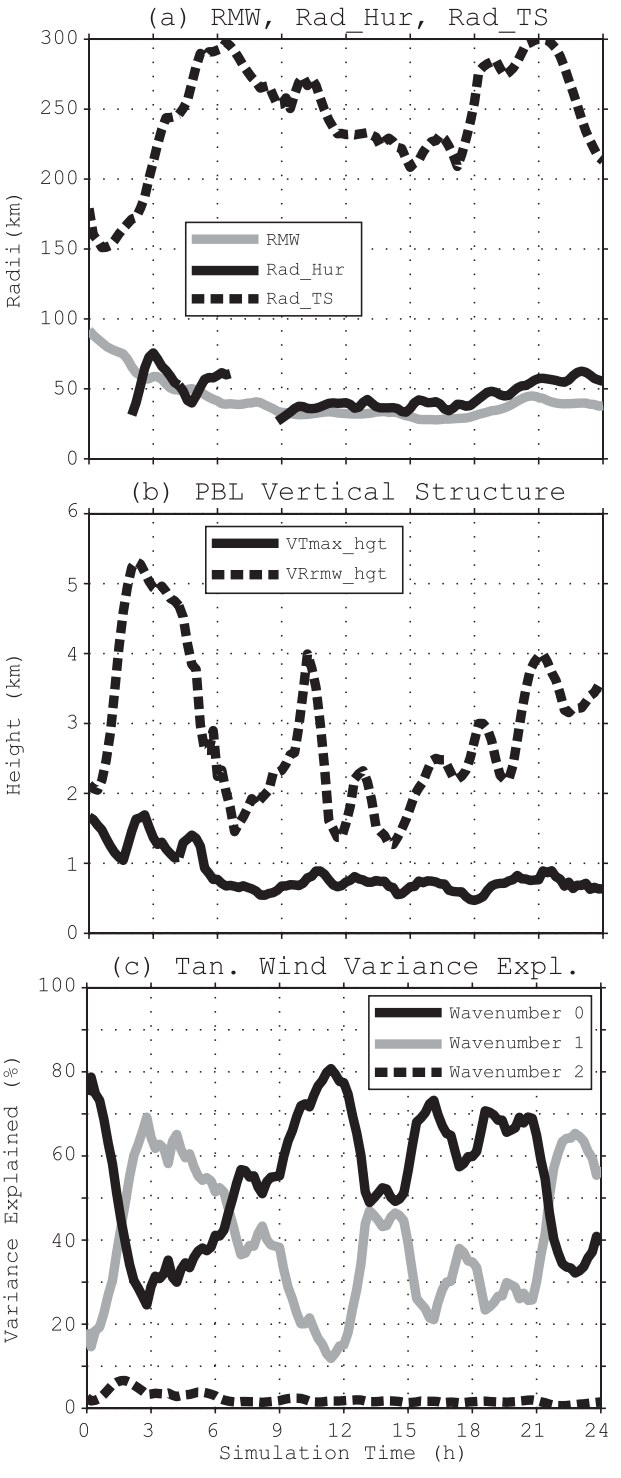

FIG. 5. Diagnostics of the vortex structure for the nature run simulation. (a) RMW (solid gray line), Rad_Hur (solid black line), and Rad_TS (dotted black line). (b) PBL vertical structure as diagnosed by VTmax_hgt (solid black line) and VRrmw_hgt (dotted black line). (c) Variance explained for the wavenumber components of tangential wind speed (solid gray line: wavenumber 0; solid black line: wavenumber 1; dotted black line: wavenumber 2).

[1] RMW here is computed at the height at which the overall azimuthally averaged VT is at a maximum at each time. While this is different than some of the other studies in the literature that use a fixed height to compute RMW, this does not introduce a large uncertainty here because the height of the overall azimuthally averaged VT itself is relatively steady throughout most of the simulation (see discussion in next paragraph).

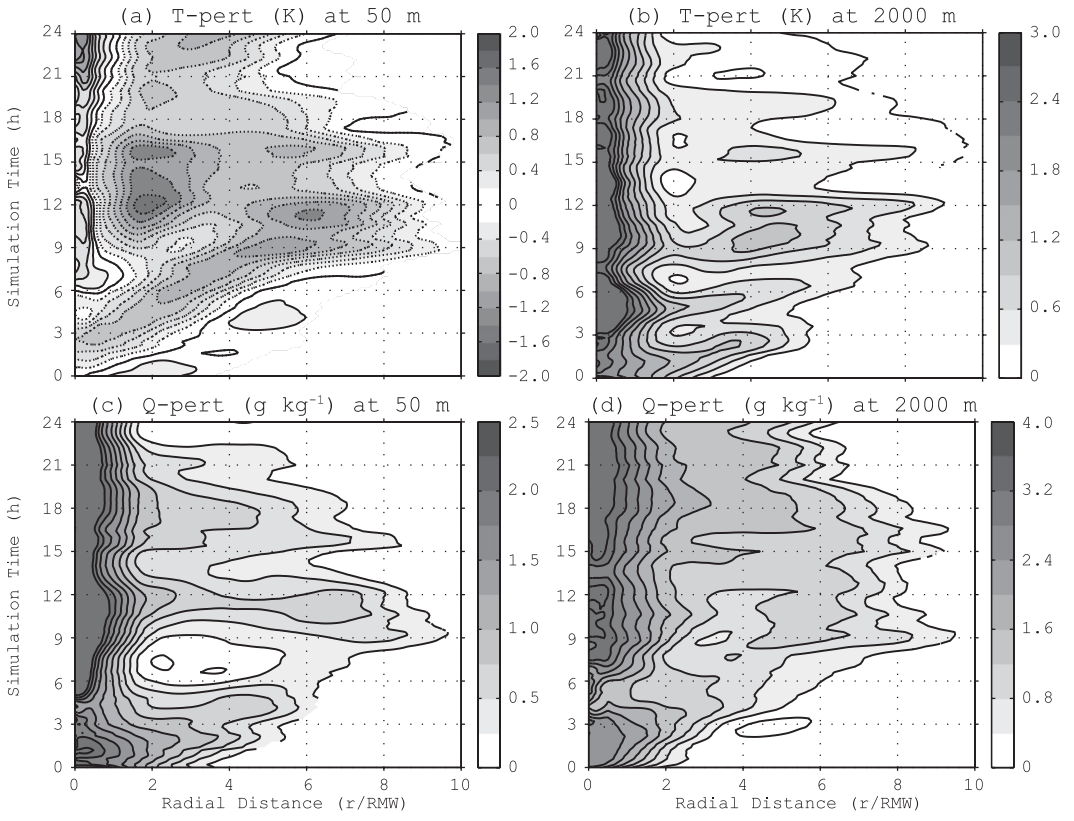

FIG. 6. Hovmöller diagrams of perturbations of (a),(b) temperature and (c),(d) specific humidity at (a),(c) 50-m and (b),(d) 2000-m height in the nature run simulation as a function of radial distance from storm center. Positive (negative) contours are plotted with solid (dotted) black lines. Simulation time increases along increasing y axes. Radial distance (normalized by RMW) is plotted along x axes. All perturbations are computed with respect to azimuthally averaged environmental values at 300-km radial distance.

Diagnostics of the simulated storm's planetary boundary layer (PBL) structure are shown in Fig. 5b. The height of the maximum azimuthally averaged tangential wind speed (VTmax_hgt) exhibits a gradual decrease during the first 9 h, with distinct fluctuations especially in the first 6 h. VTmax_hgt then settles to near 750 m throughout the rest of the simulation. The depth of the inflow layer at RMW (VRrmw_hgt) remains relatively large (2–4 km) throughout the simulation, accompanied with fluctuations as large as 3 km especially during the first half of the simulation.[2]

Finally, the variance explained by wavenumbers-0–2 components of the tangential wind speed at 2-km height is computed to show the azimuthal structure of the primary circulation in the PBL. Though the tangential wind speed is generally dominated by its wavenumber-0 component (it explains over 50% of the variance more than half of the time), large fluctuations in this quantity are observed in the first ~9 h, when a large wavenumber-1 asymmetry develops quickly from an initially mostly symmetric vortex. Axisymmetrization of the vortex gradually occurs during the second half of the simulation, but the energy in the primary circulation continues to fluctuate between the wavenumber-0 and wavenumber-1 components.[3]

3) THERMODYNAMIC STRUCTURE

The thermodynamic properties of the vortex are evaluated in Fig. 6. Specifically, the focus is on the time evolution of the radial variation of perturbations of temperature (T) and specific humidity (q) near the surface (50 m) and

[2] The inflow layer is the shallow near-surface part of the observed secondary circulation of an azimuthally averaged vortex that points radially toward the storm center.

[3] The wavenumber decomposition critically depends on the fidelity of the storm position. The storm position calculation methodology is generally robust, but there is nevertheless a degree of variability introduced because of the high resolution of the nature run, which could impact the partitioning of different components of the wind.

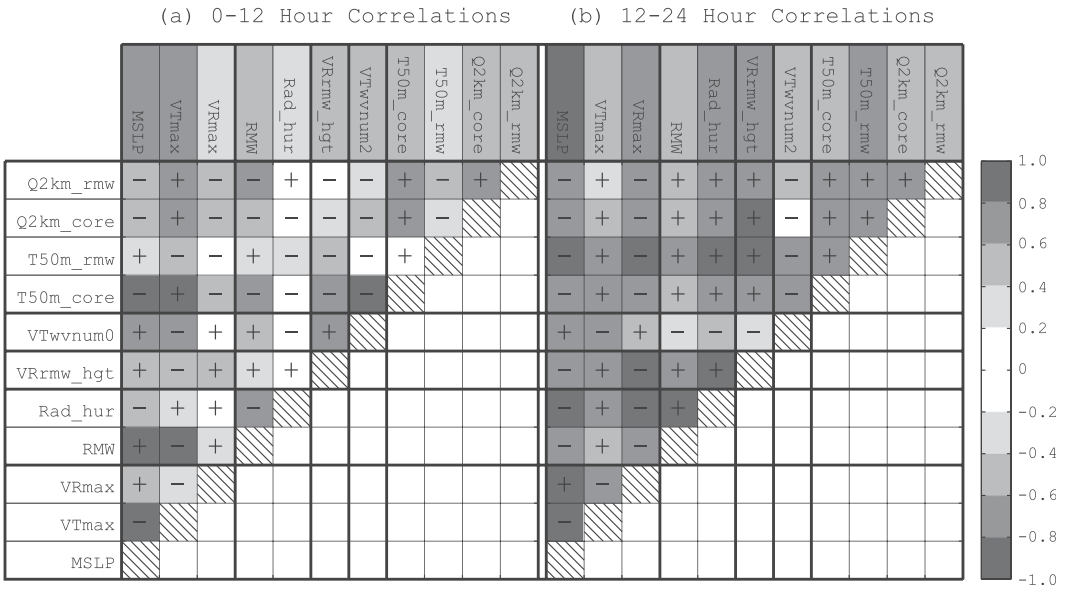

FIG. 7. Time series of correlations among various variables (r_{ij}) discussed in the text in (a) 0–12 h of the nature run simulation and (b) 12–24 h of the nature run simulation. Plus and minus symbols in boxes indicate the sign of respective correlations. Shading in the variable name boxes represents the value of average absolute correlation of a given variable with all other variables ($\bar{r}_i$). Self correlations (always equal to +1) are indicated by striped patterns along the diagonals. Variables are sorted and grouped (by thicker lines) in the order they are presented and discussed in the text.

higher in the PBL (2 km). Radial distance is normalized by RMW at each time. Perturbations are from respective azimuthally averaged environmental values at a radial distance of 300 km from the storm center.

Near the surface and inside the RMW, positive near-surface temperature perturbations are established after ~6 h but remain relatively weak, while the same region consistently experiences the largest positive moisture perturbations (2.5 g kg^{-1} or more). Meanwhile, outside the RMW, the appearance of negative temperature perturbations is collocated with convection in the eyewall and rainbands (not shown). The fast contraction of RMW in the first 12 h results in the appearance of radial expansion of the cold perturbations in the RMW-relative coordinate system.

At 2-km height, both within the RMW and outside, the vortex is dominated by positive temperature and moisture perturbations throughout the simulation. Consistent with the warm-core structure of a hurricane, positive temperature perturbations are mostly confined inside the RMW after 12 h. Meanwhile, relatively large moisture perturbations are seen throughout the simulation at radial distances of up to 6 RMW, indicative of the impact of rainbands–convective cells in moistening the atmosphere.

4) TIME CORRELATIONS AMONG VARIABLES

To better understand the dynamical connections within the vortex and to further analyze the transition from spinup to an intense model vortex, time correlations are investigated among the time series of several of the variables (r_{ij}), where i and j represent two variables. In Fig. 7, correlation computations are shown separately for the first and second halves of the simulation. Also, average absolute correlations between each variable and all other variables ($\bar{r}_i$) are shown. For brevity, only variables that exhibit relatively large correlations with others are presented.

The first noteworthy observation is the overall greater values of $\bar{r}_i$ during the second half of the simulation, which is generally interpreted as a sign of a dynamically coherent vortex. This period will hereafter be denoted as the ''mature phase'' of vortex evolution.

MSLP appears to be the variable that most consistently exhibits high correlations with others during both the spinup and mature phases ($\bar{r}_i > 0.6$ during both periods). This indicates that MSLP can provide information on intensity as well as kinematic and thermodynamic properties of the vortex during both the spinup and mature phases of storm evolution. Similar to MSLP, VTmax is also consistently well correlated with other variables. Meanwhile, the maximum azimuthally averaged radial inflow (VRmax) exhibits strong correlations only during the second half of the simulation, likely because of the slower establishment of a secondary circulation in the simulation.

RMW is moderately correlated with other variables, but a general reversal of the sign of correlations from the spinup to the mature phase is likely due to the quick contraction of

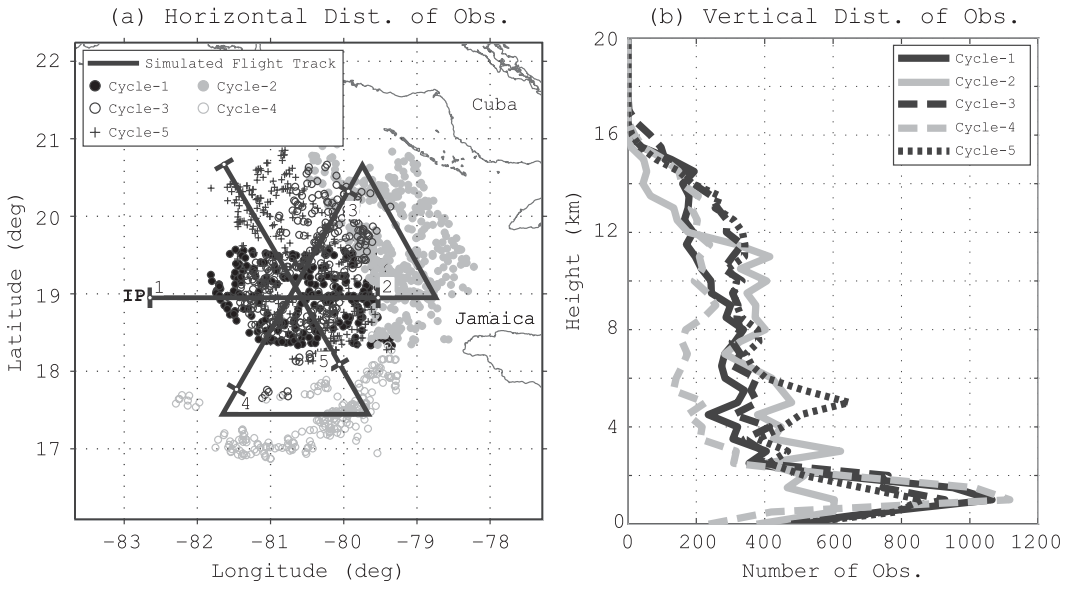

FIG. 8. (a) Simulated flight track in earth-relative coordinates and horizontal distribution of simulated Doppler wind superobs near flight level (~3-km altitude). (b) Vertical distribution of simulated Doppler wind superobs.

RMW during the spinup phase followed by the slight expansion during the mature phase. In the mature phase, Rad_Hur is highly correlated with RMW, since the radial extent of the hurricane-force winds is linked to RMW.

VRrmw_hgt exhibits some of the highest correlations to other variables, especially during the mature phase when VRrmw_hgt is positively correlated with those that indicate intensity, and exhibits a large negative correlation with VRmax. However, the positive correlation is in part due to the general increase of VRrmw_hgt during intensification (Fig. 5b) to values greater than ~1.5 km, which is typically observed in mature hurricanes in reality (J. A. Zhang et al. 2011, their Fig. 5b; Rogers et al. 2012, their Fig. 7d). Therefore, a climatology of the model itself is likely needed to assess the realism of the VRrmw_hgt evolution, which is beyond the scope of the current study.

Variance explained by the wavenumber-2 component appears to be well correlated with other variables during both phases of the nature run simulation. This suggests that, while tangential wind speed is predominantly an azimuthally symmetric quantity, its wavenumber-2 asymmetries could be a good indication of the evolution of intensity. There is a negative correlation between variance explained by the wavenumber-2 component and VTmax, similar to that shown by Nguyen et al. (2011).

5. Results

a. Data assimilation

Having established a reference of truth through the analysis of the nature run simulation, the impact of assimilating observations extracted from the 12–16-h period of the nature run is analyzed next. As demonstrated in the previous section, this period corresponds to a vortex with characteristics of a mature hurricane.

1) OBSERVATION-SPACE DIAGNOSTICS

Observation-space diagnostics are computed by accumulating various statistics of innovations, or concurrent observation-minus-forecast differences. Before assimilating observations during a particular assimilation window, they are randomly separated into two equal-volume groups. One group is used in data assimilation, and the other group is used to compute diagnostics. Both groups represent physically the same region of the vortex that was observed during a particular assimilation window. A detailed explanation of the types of observation-space diagnostics discussed here can be found in Aksoy et al. (2009). One deviation here is that "RMS innovations" are not computed by subtracting the mean innovation as in Aksoy et al. (2009), but in a traditional sense as described in Wilks [2006, his Eq. (7.53)].

The horizontal and vertical distributions of observations are shown in Fig. 8. The distribution at flight level (~3 km) where the horizontal extent of observations is greatest because of the radar scanning geometry is shown (Fig. 8a). The time windows roughly allow observations to be distributed into penetration and downwind legs. Because of the thresholding through cloud water content, the distribution is not homogeneous across the vortex and there are big data gaps in the southern and western parts of the storm where precipitation is limited or nonexistent

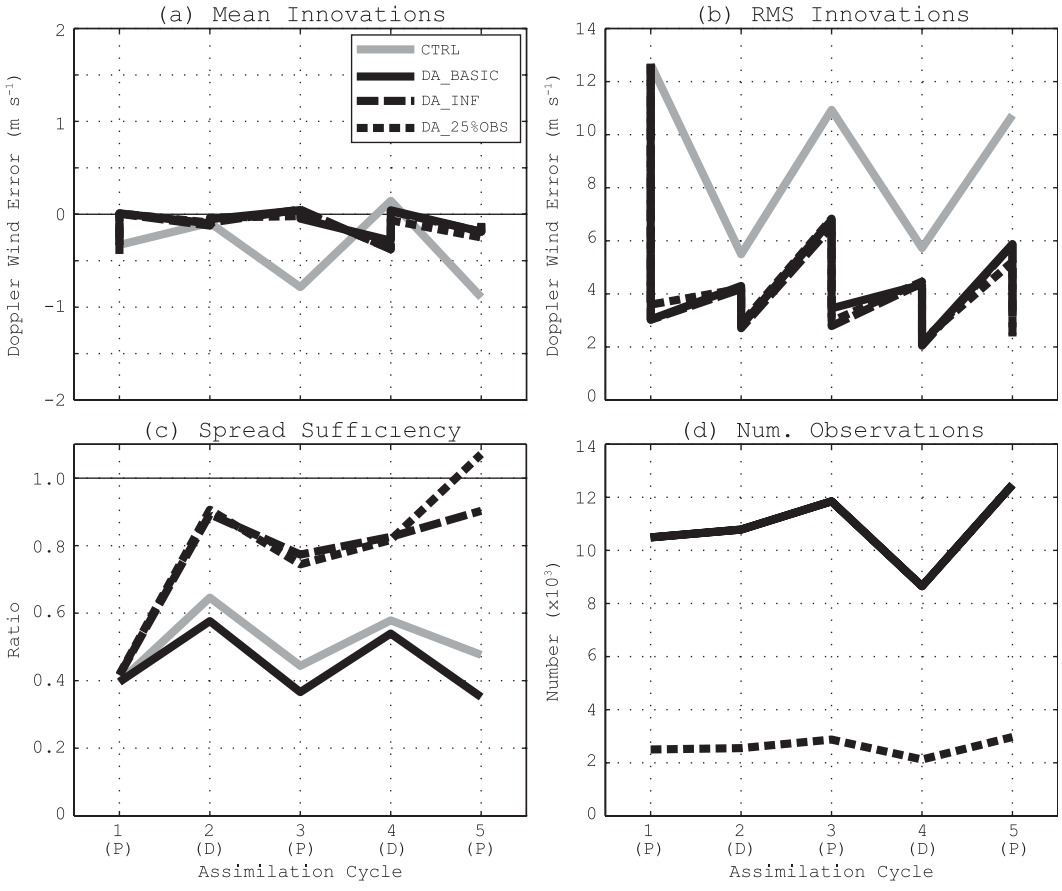

FIG. 9. Observation-space diagnostics for Doppler radial wind observations: (a) Mean innovations, (b) RMS innovations, (c) spread sufficiency, and (d) number of observations assimilated. For (a)–(c), statistics are computed at randomly selected locations that were not assimilated but were within the same respective flight legs as the assimilated observations (see the text for more details).

(cf. Fig. 13d for the distribution of total cloud mass). There are also some differences in the vertical distribution (Fig. 8b) among assimilation cycles, but the greatest observation density is generally in the boundary layer.

Observation-space diagnostics for filter performance are shown in Fig. 9, where various statistics of the prior (forecast) and posterior (analysis) innovations of Doppler radial wind are plotted for each of the assimilation cycles. Innovations in the control run (solid gray) are generally random in nature, as mean innovations are much smaller in magnitude than RMS innovations. Nevertheless, generally larger RMS and mean innovations are apparent during penetration cycles (1, 3, 5) compared to downwind leg cycles (2, 4). This is mainly due to the generally greater wind speed values during penetration cycles compared to downwind legs, as there are no other distinct differences in terms of the spatial distribution (Fig. 8) or total amount (Fig. 9d) of data.

When observations are assimilated, a noticeable reduction in RMS and mean innovations occurs. It is worthwhile to note that both penetration and downwind legs have a positive impact on innovations.

A quantitative diagnosis of ensemble spread in EnKF applications is as important as the analysis error itself because underdispersive ensembles are prone to filter divergence. Filter divergence occurs when a data assimilation system begins to assign too much weight to the background state as, by design, it interprets small ensemble spread as high confidence in the background state. This naturally results in new observations being given too little weight during the update cycle and the analysis state to resemble the background. Repeated occurrence of this phenomenon during cycling gradually accumulates forecast error and the analysis irrecoverably diverges from reality. There are fundamental reasons for the existence of spread deficiency such as limited ensemble size, sampling error, and lack of representation of model error in the ensemble, and mesoscale ensemble data assimilation systems are especially known to be prone to such issues (Meng and Zhang

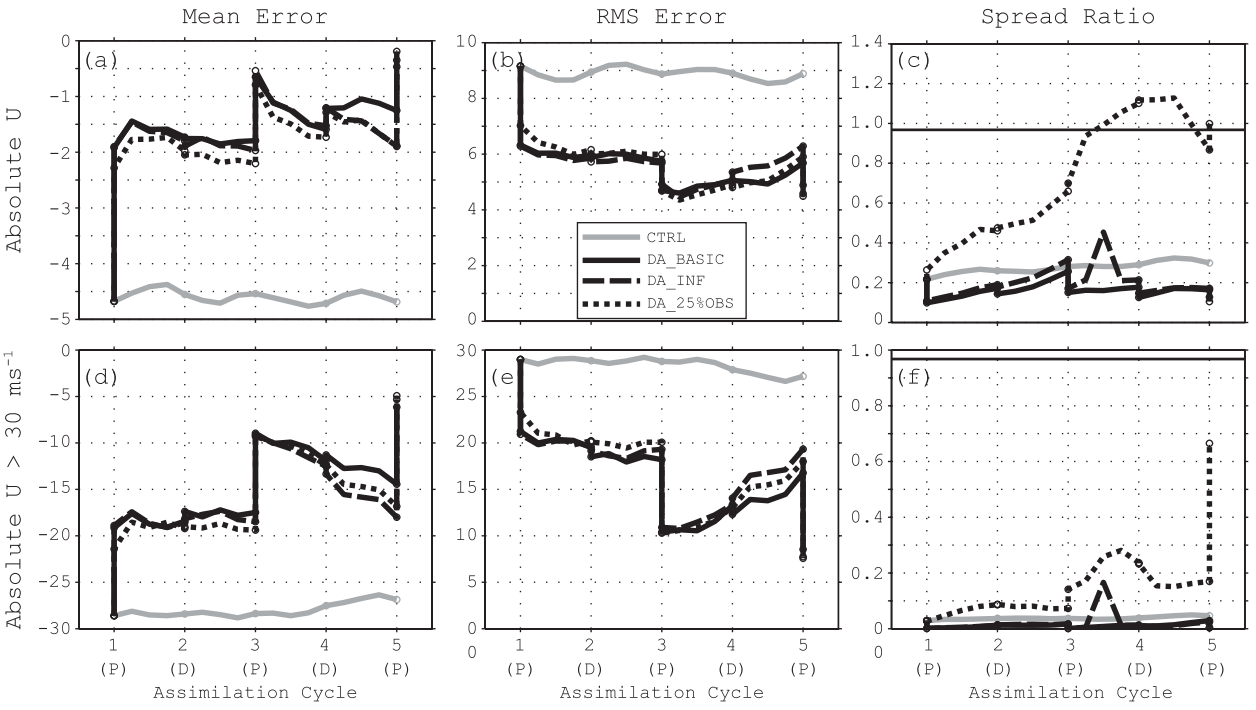

FIG. 10. Model-space comparison to the nature run for (a)–(c) all absolute u components of horizontal wind and (d)–(f) absolute u component of horizontal wind >30 m s^{-1} in the nature run. Statistics shown are (a),(d) mean error, (b),(e) RMS error, and (c),(f) spread ratio. Computations are performed in storm-relative coordinates within 300 km radially of respective storm centers.

2011). Diagnosing ensemble spread therefore needs to be a central aspect of the overall evaluation of an ensemble data assimilation system.

An interesting result is obtained in the response of ensemble spread to the various experiments performed. Ensemble spread is analyzed through "spread sufficiency" (Fig. 9c), which mainly measures how ensemble variability compares to random error (Aksoy et al. 2009). In an optimal ensemble that accurately reflects forecast errors, a general correspondence of ensemble spread (standard deviation) and random (RMS) error is expected and therefore spread sufficiency should be close to 1. When the ratio deviates to below 1, the variability in the forecast ensemble is insufficient to explain the random innovation error. Figure 9c presents a control ensemble that is suboptimal in this regard. The DA_BASIC experiment also yields comparable spread sufficiency throughout the assimilation. This implies that the expected decrease in analysis ensemble spread at assimilation times (not shown) is compensated for by sufficient ensemble variability that is introduced during short-range forecasts. Meanwhile, even as both the DA_INF and DA_25%OBS experiments experience greater ensemble spread, no improvement in error reduction is achieved (Fig. 9b). Clearly, neither applying covariance inflation nor thinning the observations (by assimilating fewer observations or reducing potential error correlation among observations) seems to reduce systematic errors in the ensemble.

2) MODEL-SPACE DIAGNOSTICS

Diagnostics in the model space provide a broader picture of the impact of data assimilation on unobserved model variables and specific features of vortex structure.

A direct comparison of model variables is performed by computing the mean and RMS errors as well as a spread ratio, in reference to the nature run. Statistics are computed in storm-relative cylindrical coordinates (0–300 km radially at 1-km resolution, 0°–360° azimuthally at 1° resolution, and 1–20 model levels vertically through the midtroposphere). Spread ratio is computed as in Snyder and Zhang (2003), and the optimal ratio of $N_e/(N_e + 1)$, where N_e represents ensemble size, is also plotted.

Figure 10 shows errors of *absolute* zonal wind ($|u|$), intended as a proxy for intensity (Figs. 10a–c). (The zonal wind u is used here for convenience as, in HEDAS, ensemble spread is only diagnosed for the prognostic model variables.) Unlike what is seen in the observation-space diagnostics, large mean error is now detected in the control run, indicating potential negative intensity bias (underprediction of intensity). Assimilation of observations

reduces the bias to less than 1 m s^{-1} in the final analysis. The control run also exhibits RMS errors of comparable magnitude to the bias. However, the reduction in RMS error when observations are assimilated is smaller than the reduction in bias. The spread ratio is also suboptimal—only about 20%–30% of its expected optimal value both in the control run and DA_BASIC experiment.

A similar but much more severe picture arises for the tail of the $|u|$ distribution (Figs. 10d–f). A threshold of 30 m s^{-1} is chosen so that only 2%–3% of the total u population of the nature run is considered, roughly corresponding to outliers of twice the standard deviation or more. A very large negative mean error in the control run (almost equal in magnitude to the 30 m s^{-1} threshold) implies that the control run does not contain a vortex of hurricane intensity. It should be noted here, however, that the spatial distribution of such extreme values is naturally localized (not shown). Therefore, the magnitude of the mean error could arise from magnitude underprediction as well as location mismatches. As will be discussed later in more detail, comparable magnitudes of mean error in the control run are also observed in the 10-m maximum wind speed parameter (see Fig. 12c), which is only impacted by the underprediction of intensity. Thus it is inferred that most of the mean error in $|u|$ greater than 30 m s^{-1} in the control run arises from the underprediction of intensity.

Meanwhile, the assimilation of observations in DA_BASIC reduces mean and RMS error magnitudes to near 5 m s^{-1} in the final analysis, despite the very low values of spread ratio. Overall, the performance of HEDAS is as good, if not better, for $|u|$ greater than 30 m s^{-1} compared to all $|u|$. We believe that this is likely due to the very good azimuthal sampling of the strongest portions of the vortex near the storm center, a natural outcome of flight geometry.

For the rest of the model fields shown here, the focus is on the tail of distributions (Fig. 11), with the assumption that they will reflect HEDAS performance in the strongest regions of the vortex. In each case, a threshold value is applied that retains the greatest 2%–3% of the values in the respective nature run population. Updraft speeds greater than 1 m s^{-1} (Figs. 11a–c) appear to exhibit ~ -1.5 m s^{-1} mean error and ~ 2 m s^{-1} RMS error in the control run. Vertical wind speed is not a direct analysis variable in the HEDAS system (because it is not a prognostic variable in HWRF). In the DA_BASIC experiment, a slight improvement of ~ 0.2 m s^{-1} in the mean error persists through the cycles, indicating that an improvement in the kinematic structure also leads to somewhat stronger updrafts in the model during cycling. However, large errors remain even after data assimilation, implying that they are due to systematic model differences between the nature run and the ensemble, horizontal resolution likely being a major contributor.

Thermodynamic properties are measured by comparing temperature and specific humidity perturbations (Figs. 11d–i), where perturbations are computed as in section 4c(3), computed separately for each model level. Both temperature and specific humidity perturbations indicate that ensemble runs (without and with data assimilation) are cooler and less moist than the nature run. Large RMS errors are also apparent in the control run. It should be noted that the impact of data assimilation on the thermal structure is indirect through ensemble correlations, as observations only contain wind information. Data assimilation helps improve the thermal structure noticeably by as much as 2 K in both mean and RMS values. As positive temperature perturbations are associated with the warm core of a vortex, this is an indication that the assimilation of Doppler wind data indirectly has a positive impact on the representation of the warm core in the analysis. Meanwhile, the assimilation of Doppler wind information appears to lead to the worsening of mean and RMS errors of moisture perturbations. It is not clear at the moment why such a worsening should occur in specific humidity. We suspect that it is related to smaller-scale and less robust ensemble covariances of moisture with wind, which would likely result in a noisy update of moisture in HEDAS [an indication of this is found by Poterjoy and Zhang (2011)].

Total cloud water mass (CWM), which is the only microphysical variable updated in HEDAS, also exhibits large negative bias (underprediction) in the control run (Fig. 11j). This bias is partially offset by the application of the EnKF. However, improvement in the RMS error is smaller.

Ensemble variability appears to be smaller in model space for the tails of distributions (cf. spread sufficiency of ~ 0.5 in observation space in Fig. 10 to ~ 0.2 in model space in Fig. 11, as well as the smaller ratio for thresholded $|u|$ in Fig. 10c than all of $|u|$ in Fig. 10f). This hints at an ensemble that is especially underdispersive in the extreme ends of the probability distributions.

When the various data assimilation experiments are compared in model space (Figs. 10, 11, black solid, dashed, and dotted lines), the best results generally appear to be obtained from DA_BASIC, although differences are small in many cases. This result is consistent with the findings in observation space. It also suggests that ensemble underdispersion in the most convectively active regions of the vortex is likely due to the model's inability to generate sufficient error growth.

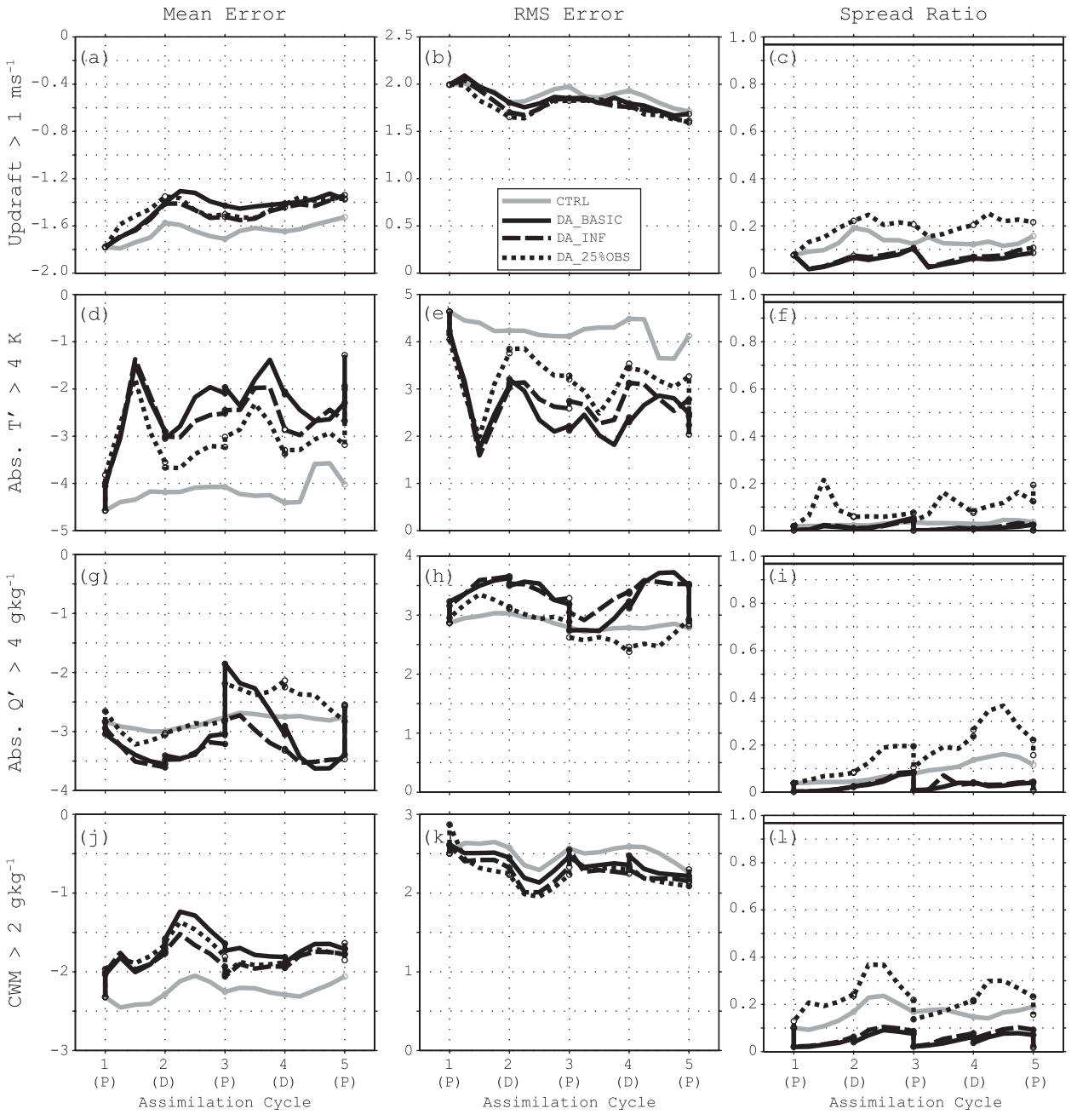

FIG. 11. As in Fig. 10, but for (a)–(c) updraft speed >1 m s^{-1}, (d)–(f) absolute perturbation temperature >4 K, (g)–(i) absolute perturbation specific humidity >4 g kg^{-1}, and (j)–(l) total CWM >2 g kg^{-1}.

Further investigation of filter performance in model space is performed for some of the parameters that were deemed relevant during the analysis of the nature run simulation. Figure 12 summarizes, for nine of these parameters, the deviations of the control and data assimilation experiments from the nature run. For better comparison, the deviation values are also computed for the ensemble mean during the 6-h spinup.

First, large deviations from the nature run are exhibited in the control run for position and intensity. Several aspects of the vortex appear to be improved when data assimilation is performed in DA_BASIC. Position error is quickly reduced from ~100 to ~20 km (Fig. 12a). Intensity is also improved to within ~2 hPa and 5 m s^{-1} of the nature run for MSLP and V10max, respectively (Figs. 12b,c). Improvement in maximum azimuthally averaged

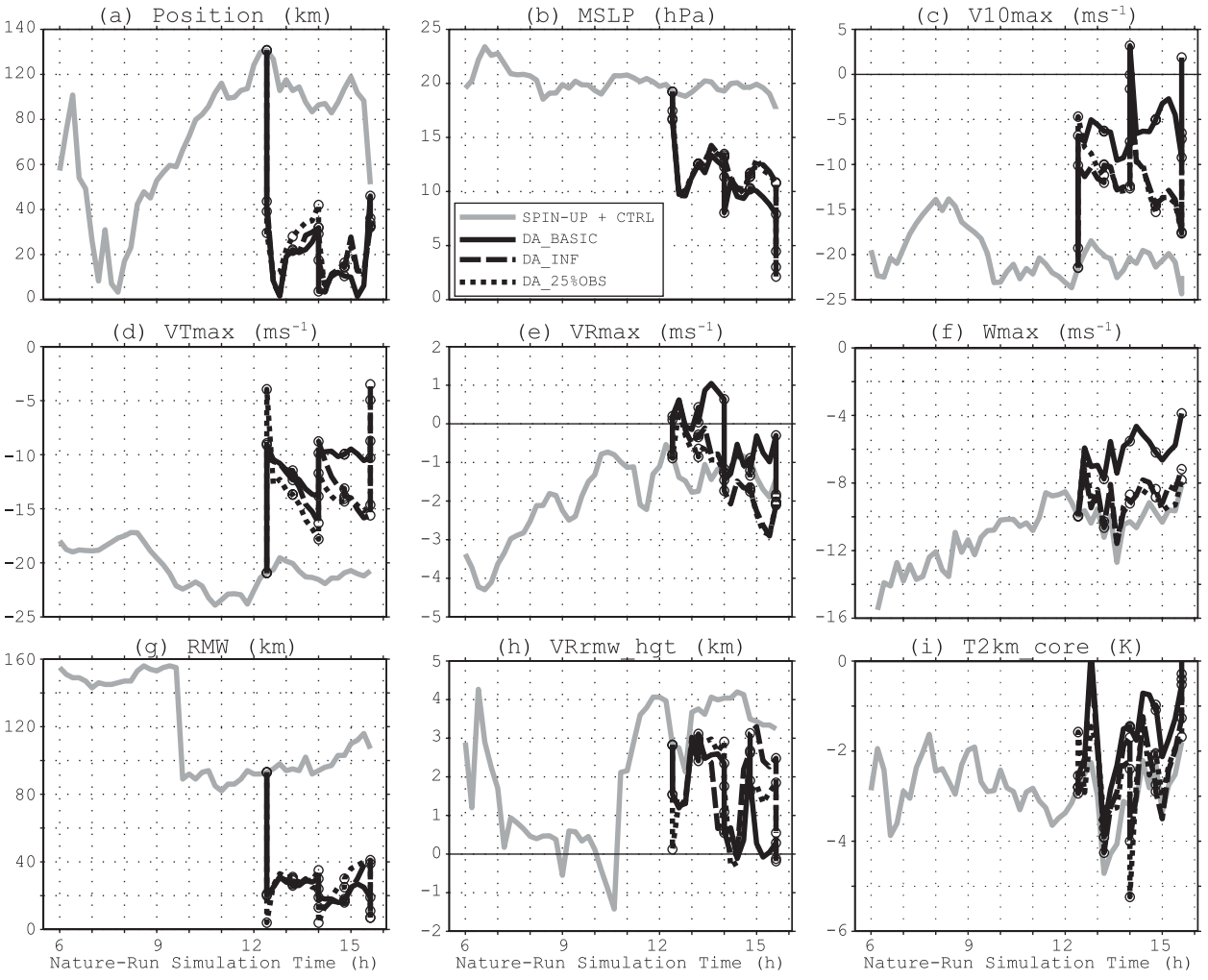

FIG. 12. Deviations of the spinup and control runs, as well as the data assimilation experiments, from the nature run for several of the parameters used to evaluate simulation in section 5a. Time along x axis denotes hours since the start of the nature run simulation.

tangential wind speed is less dramatic, but error is still reduced by 50% to ~10 m s^{-1} (Fig. 12d) in DA_BASIC.

Error in maximum azimuthally averaged inflow appears to generally be in the 1–2 m s^{-1} range, and is only slightly improved in the DA_BASIC experiment (Fig. 12e). This may partially arise from the asymmetric nature of the inflow. Observations along a single penetration cannot fully sample the asymmetry in the inflow pattern (not shown), so that the update of the inflow heavily depends on the underlying correlation structure and is likely to be impacted by the errors in the forecast model. Such behavior can therefore also be expected in other variables that exhibit azimuthal asymmetry.

Large errors in the maximum updraft speed in the control by ~10 m s^{-1} indicate severe underprediction of the intensity of convection (Fig. 12f). While errors still remain after data assimilation in DA_BASIC, a reduction by ~5 m s^{-1} suggests that improvements in the kinematic aspects of the vortex structure are ultimately translated to stronger convection.

Very impressive improvement in the RMW error suggests that Doppler wind observations contain relevant information regarding the tangential wind structure (Fig. 12g). Meanwhile, the vertical structure of the inflow appears to be hard to capture in the data assimilation system (Fig. 12h). While there are improvements at the assimilation times of the penetrations (odd-numbered cycles), subsequent short-range forecasts do not appear to maintain these shallower inflow layers in the analyses. This hints at a structural issue of the forecast model in producing deeper inflow layers relative to the nature run.

Finally, temperature perturbation within the hurricane core at 2-km height is underpredicted in the control by

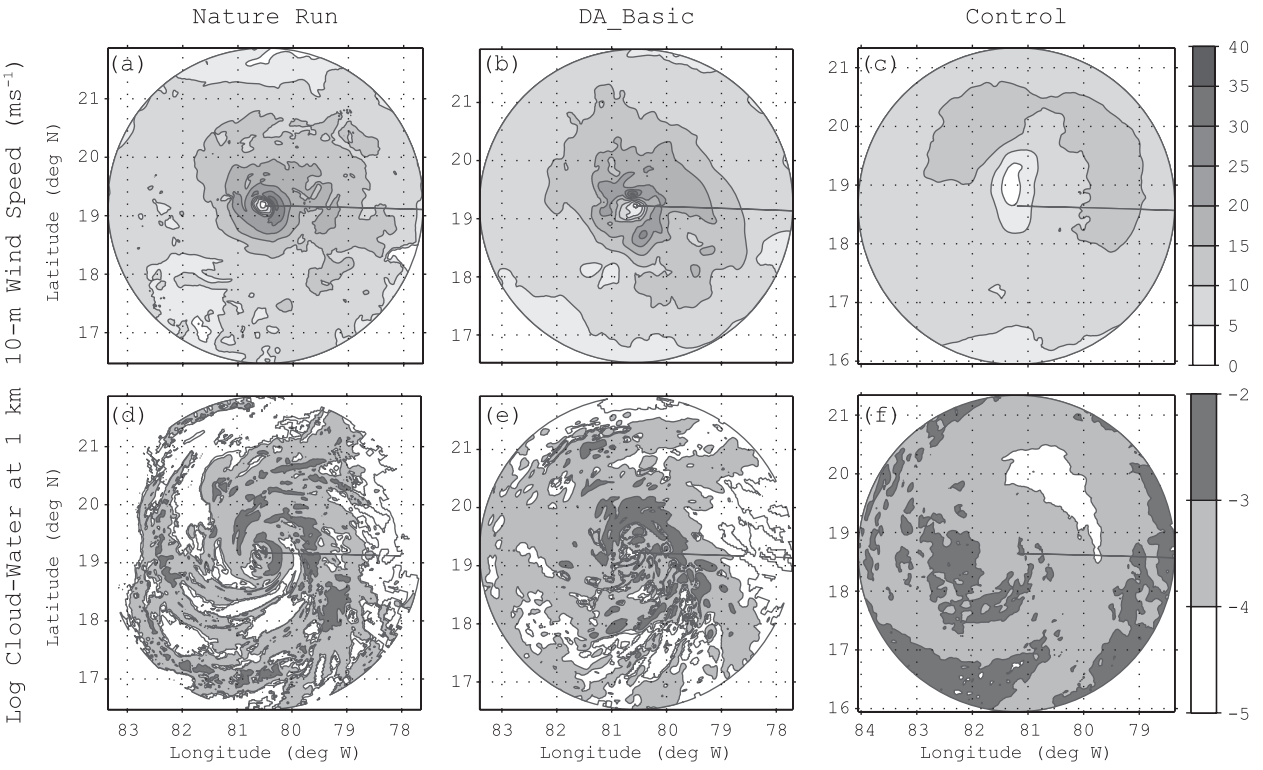

FIG. 13. (a)–(c) Storm-relative horizontal cross sections of 10-m wind speed (m s^{-1}) and (d)–(f) logarithm of 1-km total CWM in the (a),(d) nature run, (b),(e) final mean analysis in DA_BASIC experiment, and (c),(f) control.

~4 K, and data assimilation in DA_BASIC appears to result in a slight improvement (Fig. 12i). These results are generally better for temperature perturbation than for specific humidity perturbation, and better at 2-km altitude than at the surface (not shown). This suggests that, in the current HEDAS configuration, the indirect update of the thermodynamic fields is most successful for the warm-core region and likely has a positive impact on the eventual strengthening of convection in short-range forecasts.

b. *Comparison of the final analysis to the nature run*

The vortex structure obtained in the final analysis is now compared to the nature run and the control at the same time. Since the best results are generally obtained in the DA_BASIC experiment, here the focus is specifically on this experiment. Figure 13 compares storm-relative horizontal cross sections of 10-m wind speed and 1-km CWM. The general wavenumber-1 asymmetry as well as RMW is captured well in the final mean analysis, although the wind update near the core appears noisier than the truth. The horizontal distribution of CWM is also more realistic, especially when compared to the broad distribution in the control.

Figure 14 compares azimuthally averaged vertical cross sections of tangential and radial wind speeds, as well as equivalent potential temperature (θ_e). In general, the structure of tangential wind speed is captured well in the final analysis, although a general underestimation of intensity by as much as 10 m s^{-1} is apparent (cf. this result to Fig. 12d). The structure of the radial flow, too, is generally captured very well in the analysis, although the vertical structure of the inflow in the PBL is somewhat exaggerated in the final analysis. Finally, the thermal structure is also well represented in the analysis in an azimuthally averaged sense. The midlevel warm-core structure is realistic but its magnitude is somewhat overpredicted (Fig. 14h). This feature is nonexistent in the control run (Fig. 14i). Meanwhile, generally overestimated θ_e in the PBL is very similar to the values in the PBL of the control run, suggesting that the assimilation of Doppler wind observations did not have much impact on the thermal structure of the PBL.

6. Summary and discussion

In this study, NOAA/AOML/HRD's HEDAS is introduced and a preliminary analysis of the impact of airborne Doppler radar wind data is carried out in an

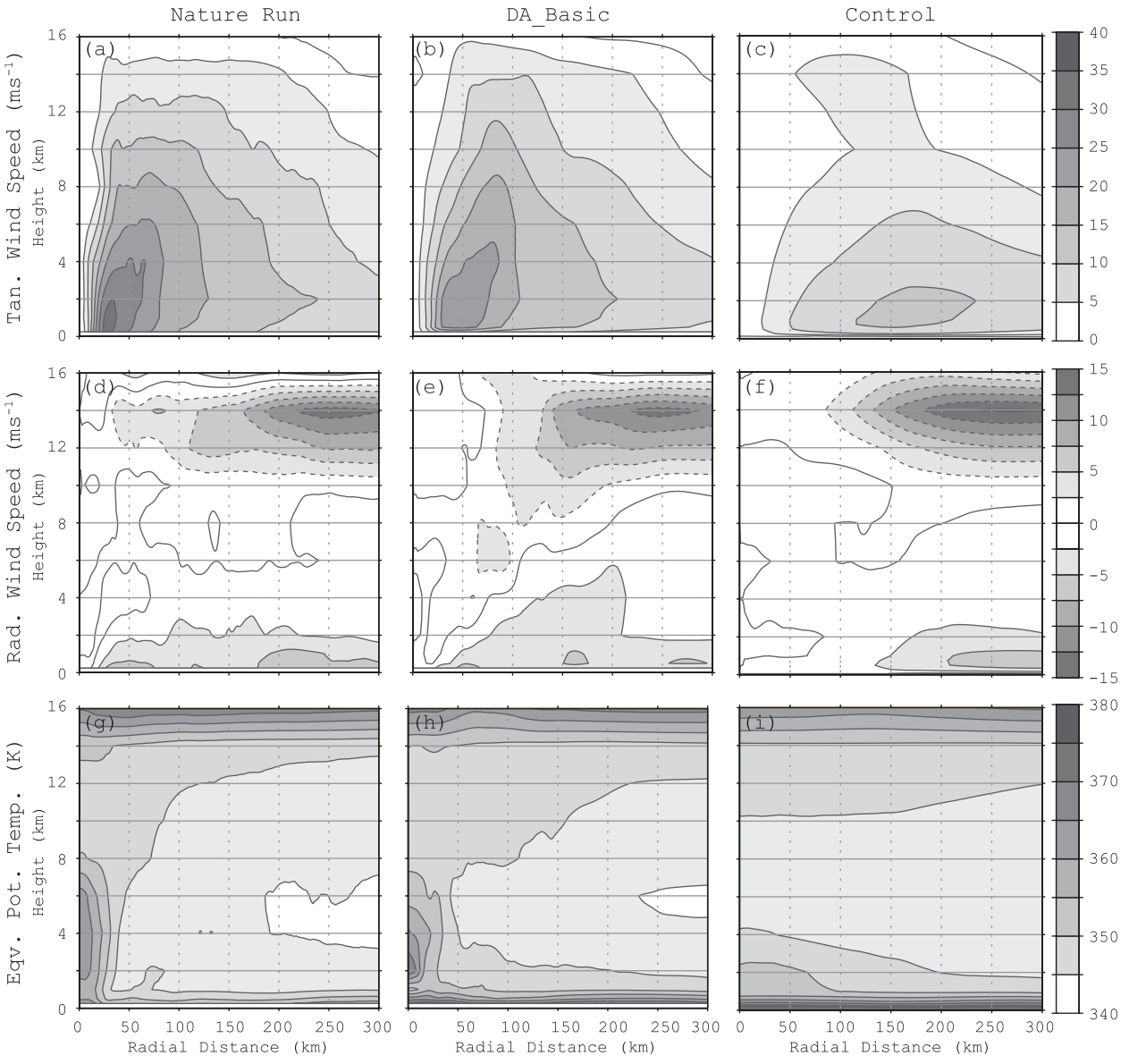

FIG. 14. Vertical cross sections of azimuthally averaged (a)–(c) tangential wind speed (m s^{-1}) and (d)–(f) radial wind speed (m s^{-1}; inflow with solid contours, outflow with dashed contours); and (g)–(i) equivalent potential temperature (K) in the (a),(d),(g) nature run, (b),(e),(h) final mean analysis in DA_BASIC experiment, and (c),(f),(i) control.

OSSE, where the nature run simulation is obtained with a higher-resolution (4.5/1.5 km horizontal grid spacing) version of experimental HWRF. This version is initialized from one member of the GFS/EnKF analysis ensemble, configured with explicit convection in all domains, and spun up for a longer time period with a vortex-following inner nest.

The 24-h nature run simulation is initialized from the 1200 UTC 7 November 2008 GFS/EnKF representation of Hurricane Paloma. The first 12 h of the simulation are generally influenced by the adjustment to the initial vortex from the much-lower-resolution global model. Indications of this adjustment are seen in the fluctuations in storm position and kinematic and thermodynamic properties of the vortex. Time correlations among various variables are also generally weak. In the second 12-h period, stronger time correlations and generally smaller fluctuations in the fields suggest that the vortex-scale dynamics have become more coherent.

During the 24-h simulation, the vortex in the nature run steadily intensifies from a tropical storm to a category-2 hurricane. Although weaker than observed during the

same period, the evolution of the vortex in the nature run is sufficiently realistic in structure. Too strong a vortex, in the presence of a weak initial vortex from the global model, would introduce large innovations and likely result in suboptimal data assimilation, whereas a weak vortex would potentially not exhibit all the relevant dynamical features by which to measure the impact of Doppler radar data.

The Doppler radar radial wind data are produced by simulating a butterfly-shaped flight pattern within the nature run during the ''mature phase'' and then interpolating from model space using a realistic forward operator. These are then processed to produce lower-resolution superobservations and assimilated using HEDAS. The impact of assimilating Doppler wind superobservations is assessed in observation space as well as in model space. In general, RMS innovations are observed to be much greater than mean innovations, while data assimilation reduces both. Errors are greater for observations in penetrations than downwind legs, likely because of much stronger winds in the inner core that are only sampled during penetrations. Furthermore, ensemble spread is only about 50% of what is expected optimally when no covariance inflation is applied. However, while covariance inflation and data thinning increase spread sufficiency to near 100%, neither leads to improvement in innovation-based performance characteristics.

In model space, too, improvements are observed when Doppler wind data are assimilated, especially in the kinematic aspects of the vortex structure; storm position, MSLP, maximum 10-m wind speed, maximum azimuthally averaged tangential wind speed, and RMW all exhibit distinct improvements over the control experiment. Meanwhile, the indirect impact on unobserved fields, especially the thermal structure, is much smaller. Nevertheless, the assimilation of Doppler wind observations results in significant improvements in the vortex structure, while underestimation of overall intensity leads to a general bias in the average error statistics.

Several aspects of these results are noteworthy. First, a general deficiency in ensemble spread is observed. More interestingly, while covariance inflation–relaxation and observation thinning result in improved ensemble spread, these do not result in improvements in overall error statistics. This is an indication of the lack of ensemble sampling in certain directions of the phase space, which generally results from model error. Indeed, the dominance of bias in certain error statistics, such as underestimation of intensity and errors in the depth of the inflow layer, does hint at the presence of model error. It appears that modifications made for the nature run contribute to significant differences between the models used in HEDAS and the nature run. Therefore, representing model error in the ensemble could be one approach to remedy the lack of ensemble spread.

Furthermore, the mixed impact of the assimilation of Doppler radar wind observations on unobserved aspects of the hurricane vortex is in itself quite interesting. Specifically, while consistent and significant improvements are observed in the kinematic fields, improvements are less consistent in the convective and thermodynamic features of the vortex. Indeed, the hydrometeor distribution from the horizontal cross section of the total cloud water field, as well as the thermodynamic structure from the vertical cross section of the azimuthally averaged equivalent potential temperature field, both indicate that data assimilation has a positive indirect impact through model dynamics during cycling. However, the fact that this is not reflected as much in domainwide average statistics is a sign that improvements are noisy in nature. This may be due to generally smaller indirect correlations between wind and other variables, as well as the smaller spatial scale of such correlations associated with the small-scale nature of convection, and suggests a need for direct observations of the thermodynamic structure (as available from flight-level and dropwindsonde observations in real P-3 flights).

Finally, Doppler wind data sampled in both penetration and downwind legs appear to positively contribute to HEDAS performance. However, data from penetrations generally have greater impact than data from downwind legs. This is likely due to better radial sampling of the vortex by penetrations as well as the ability to sample the most intense regions of the vortex during penetrations. In contrast, downwind legs only sample the outer regions of a vortex and therefore observations from downwind legs lack information on the most important characteristics of the inner core of a vortex (such as intensity, RMW, and the patterns of primary and secondary circulations) although they could potentially be providing information on the atmospheric environment that the vortex is embedded in. How to make optimal use of the combination of penetration and downwind legs is a subject of future investigation.

Acknowledgments. The authors acknowledge funding from the NOAA Hurricane Forecast Improvement Project that supported this work. This research was carried out (in part) under the auspices of CIMAS, a joint institute of the University of Miami and NOAA, Cooperative Agreement NA67RJ0149. HRD Director Dr. Frank Mark's guidance and leadership have been instrumental in the success of the HEDAS project. Dr. Zhiyong Meng and Dr. Yonghui Weng's inputs were very helpful in the early development of the EnKF code in HEDAS. We are

also grateful for the amazing support from the HRD modeling group, especially from Dr. Xuejin Zhang and Mr. Thiago Quirino. Dr. Jeff Whitaker of NOAA/ESRL has kindly provided the GFS/EnKF data. HRD scientists Dr. Rob Rogers and Dr. Paul Reasor provided very useful criticism that enhanced the manuscript. Constructive comments from two anonymous reviewers were very helpful in improving the manuscript and bringing it to its final form. Additionally, the first author wishes to acknowledge insightful discussions with Dr. Chris Snyder and Dr. Jeff Anderson throughout the HEDAS development and testing phase.

REFERENCES

Aberson, S. D., 2010: 10 years of hurricane synoptic surveillance (1997–2006). *Mon. Wea. Rev.,* **138,** 1536–1549.

——, M. L. Black, R. A. Black, R. W. Burpee, J. J. Cione, C. W. Landsea, and F. D. Marks Jr., 2006: Thirty years of tropical cyclone research with the NOAA P-3 aircraft. *Bull. Amer. Meteor. Soc.,* **87,** 1039–1055.

Aksoy, A., D. Dowell, and C. Snyder, 2009: A multicase comparative assessment of the ensemble Kalman filter for assimilation of radar observations. Part I: Storm-scale analyses. *Mon. Wea. Rev.,* **137,** 1805–1824.

——, ——, and ——, 2010: A multicase comparative assessment of the ensemble Kalman filter for assimilation of radar observations. Part II: Short-range ensemble forecasts. *Mon. Wea. Rev.,* **138,** 1273–1292.

Atlas, R., 1997: Atmospheric observations and experiments to assess their usefulness in data assimilation. *J. Meteor. Soc. Japan,* **75,** 111–130.

Bender, M. A., I. Ginnis, R. Tuleya, B. Thomas, and T. Marchok, 2007: The operational GFDL coupled hurricane–ocean prediction system and a summary of its performance. *Mon. Wea. Rev.,* **135,** 3965–3989.

Berg, R. J., and L. A. Avila, 2011: Annual summary: Atlantic hurricane season of 2009. *Mon. Wea. Rev.,* **139,** 1049–1069.

Black, M. L., R. W. Burpee, and F. D. Marks Jr., 1996: Vertical motion characteristics of tropical cyclones determined with airborne Doppler radial velocities. *J. Atmos. Sci.,* **53,** 1887–1909.

Brown, D. P., J. L. Beven, J. L. Franklin, and E. S. Blake, 2010: Annual summary: Atlantic hurricane season of 2008. *Mon. Wea. Rev.,* **138,** 1975–2001.

Chapman, B., G. Jost, and R. van der Pas, 2007: *Using OpenMP. Portable Shared Memory Parallel Programming*. The MIT Press, 353 pp.

Chen, S. S., J. F. Price, W. Zhao, M. A. Donelan, and E. J. Walsh, 2007: The CBLAST-Hurricane Program and the next-generation fully coupled atmosphere–wave–ocean models for hurricane research and prediction. *Bull. Amer. Meteor. Soc.,* **88,** 311–317.

Dowell, D. C., F. Zhang, L. J. Wicker, C. Snyder, and N. A. Crook, 2004: Wind and temperature retrievals in the 17 May 1981 Arcadia, Oklahoma, supercell: Ensemble Kalman filter experiments. *Mon. Wea. Rev.,* **132,** 1982–2005.

——, L. J. Wicker, and C. Snyder, 2011: Ensemble Kalman filter assimilation of radar observations of the 8 May 2003 Oklahoma City supercell: Influences of reflectivity observations on storm-scale analyses. *Mon. Wea. Rev.,* **139,** 272–294.

Dudhia, J., 1989: Numerical study of convection observed during the winter monsoon experiment using a mesoscale two-dimensional model. *J. Atmos. Sci.,* **46,** 3077–3107.

Ek, M. B., K. E. Mitchell, Y. Lin, E. Rogers, P. Grunmann, V. Koren, G. Gayno, and J. D. Tarpley, 2003: Implementation of Noah land surface model advances in the National Centers for Environmental Prediction operational mesoscale Eta model. *J. Geophys. Res.,* **108,** 8851, doi:10.1029/2002JD003296.

Evensen, G., 1994: Sequential data assimilation with a nonlinear quasigeostrophic model using Monte Carlo methods to forecast error statistics. *J. Geophys. Res.,* **99** (C5), 10 143–10 162.

Ferrier, B. S., Y. Jin, Y. Lin, T. Black, E. Rogers, and G. DiMego, 2002: Implementation of a new grid-scale cloud and precipitation scheme in the NCEP Eta model. Preprints, *15th Conf. on Numerical Weather Prediction,* San Antonio, TX, Amer. Meteor. Soc., 280–283.

Gamache, J. F., F. D. Marks Jr., and F. Roux, 1995: Comparison of three airborne Doppler sampling techniques with airborne in situ wind observations in Hurricane Gustav (1990). *J. Atmos. Oceanic Technol.,* **12,** 171–181.

Gaspari, G., and S. E. Cohn, 1999: Construction of correlation functions in two and three dimensions. *Quart. J. Roy. Meteor. Soc.,* **125,** 723–757.

Gopalakrishnan, S. G., and Coauthors, 2002: An operational multiscale hurricane forecasting system. *Mon. Wea. Rev.,* **130,** 1830–1847.

——, N. Surgi, R. Tuleya, and Z. Janjic, 2006: NCEP's two-way-interactive-moving-nest NMM-WRF modeling system for hurricane forecasting. Preprints, *27th Conf. on Hurricanes and Tropical Meteorology,* Monterey, CA, Amer. Meteor. Soc., 7A.3. [Available online at http://ams.confex.com/ams/pdfpapers/107899.pdf.]

——, F. Marks Jr., X. Zhang, J.-W. Bao, K.-S. Yeh, and R. Atlas, 2011: The experimental HWRF system: A study on the influence of horizontal resolution on the structure and intensity changes in tropical cyclones using an idealized framework. *Mon. Wea. Rev.,* **139,** 1762–1784.

Hamill, T. M., and J. S. Whitaker, 2005: Accounting for the error due to unresolved scales in ensemble data assimilation: A comparison of different approaches. *Mon. Wea. Rev.,* **133,** 3132–3147.

——, ——, M. Fiorino, and S. G. Benjamin, 2011: Global ensemble predictions of 2009's tropical cyclones initialized with an ensemble Kalman filter. *Mon. Wea. Rev.,* **139,** 668–688.

Hong, S.-Y., and H.-L. Pan, 1996: Nonlocal boundary layer vertical diffusion in a medium-range forecast model. *Mon. Wea. Rev.,* **124,** 2322–2339.

——, and ——, 1998: Convective trigger function for a mass-flux cumulus parameterization scheme. *Mon. Wea. Rev.,* **126,** 2599–2620.

Houtekamer, P. L., and H. L. Mitchell, 1998: Data assimilation using an ensemble Kalman filter technique. *Mon. Wea. Rev.,* **126,** 796–811.

Houze, R. A., S. S. Chen, B. F. Smull, W.-C. Lee, and M. M. Bell, 2007: Hurricane intensity and eyewall replacement. *Science,* **315,** 1235–1238.

Kalnay, E., 2003: *Atmospheric Modeling, Data Assimilation, and Predictability.* Cambridge University Press, 341 pp.

Kaplan, J., M. DeMaria, and J. A. Knaff, 2010: A revised tropical cyclone rapid intensification index for the Atlantic and eastern North Pacific basins. *Wea. Forecasting,* **25,** 220–241.

Mallen, K. J., M. T. Montgomery, and B. Wang, 2005: Reexamining the near-core radial structure of the tropical cyclone primary

circulation: Implications for vortex resiliency. *J. Atmos. Sci.,* **62,** 408–425.

Meng, Z., and F. Zhang, 2011: Limited-area ensemble-based data assimilation. *Mon. Wea. Rev.,* **139,** 2025–2045.

Mlawer, E. J., S. J. Taubman, P. D. Brown, M. J. Iacono, and S. A. Clough, 1997: Radiative transfer for inhomogeneous atmospheres: RRTM, a validated correlated-k model for the longwave. *J. Geophys. Res.,* **102** (D14), 16 663–16 682.

Moon, I.-J., I. Ginnis, T. Hara, and B. Thomas, 2007: A physics-based parameterization of air–sea momentum flux at high wind speeds and its impact on hurricane intensity predictions. *Mon. Wea. Rev.,* **135,** 2869–2878.

Nguyen, M. C., M. J. Reeder, N. E. Davidson, R. K. Smith, and M. T. Montgomery, 2011: Inner-core vacillation cycles during the intensification of Hurricane Katrina. *Quart. J. Roy. Meteor. Soc.,* **137,** 829–844.

Nguyen, S. V., R. K. Smith, and M. T. Montgomery, 2008: Tropical-cyclone intensification and predictability in three dimensions. *Quart. J. Roy. Meteor. Soc.,* **134,** 563–582.

Poterjoy, J., and F. Zhang, 2011: Dynamics and structure of forecast error covariance in the core of a developing hurricane. *J. Atmos. Sci.,* **68,** 1586–1606.

Pu, Z., X. Li, and J. Sun, 2009: Impact of airborne Doppler radar data assimilation on the numerical simulation of intensity changes of Hurricane Dennis near a landfall. *J. Atmos. Sci.,* **66,** 3351–3365.

Rappaport, E. N., and Coauthors, 2009: Advances and challenges at the National Hurricane Center. *Wea. Forecasting,* **24,** 395–419.

Reasor, P. D., M. T. Montgomery, and L. D. Grasso, 2004: A new look at the problem of tropical cyclones in vertical shear flow: Vortex resiliency. *J. Atmos. Sci.,* **61,** 3–22.

Rogers, R., 2010: Convective-scale structure and evolution during a high-resolution simulation of tropical cyclone rapid intensification. *J. Atmos. Sci.,* **67,** 44–70.

——, S. Lorsolo, P. Reasor, J. Gamache, and F. Marks, 2012: Multiscale analysis of tropical cyclone kinematic structure from airborne Doppler radar composites. *Mon. Wea. Rev.,* **140,** 77–99.

Snyder, C., and F. Zhang, 2003: Assimilation of simulated Doppler radar observations with an ensemble Kalman filter. *Mon. Wea. Rev.,* **131,** 1663–1677.

Weng, Y., and F. Zhang, 2012: Assimilating airborne Doppler radar observations with an ensemble Kalman filter for convection-permitting hurricane initialization and prediction: Katrina (2005). *Mon. Wea. Rev.,* **140,** 841–859.

Whitaker, J., and T. M. Hamill, 2002: Ensemble data assimilation without perturbed observations. *Mon. Wea. Rev.,* **130,** 1913–1924.

Wilks, D. S., 2006: *Statistical Methods in the Atmospheric Sciences*. 2nd ed. Academic Press, 627 pp.

Xiao, Q., Y.-H. Kuo, J. Sun, W.-C. Lee, D. Barker, and E. Lim, 2007: An approach of radar reflectivity data assimilation and its assessment with the inland QPF of Typhoon Rusa (2002) at landfall. *J. Appl. Meteor. Climatol.,* **46,** 14–22.

——, Z. Zhang, C. Davis, J. Tuttle, G. Holland, and P. J. Fitzpatrick, 2009: Experiments of hurricane initialization with airborne Doppler radar data for the Advanced Research Hurricane WRF (AHW) model. *Mon. Wea. Rev.,* **137,** 2758–2777.

Zhang, F., C. Snyder, and J. Sun, 2004: Impacts of initial estimate and observation availability on convective-scale data assimilation with an ensemble Kalman filter. *Mon. Wea. Rev.,* **132,** 1238–1253.

——, Y. Weng, J. A. Sippel, Z. Meng, and C. Bishop, 2009: Cloud-resolving hurricane initialization and prediction through assimilation of Doppler radar observations with an ensemble Kalman filter. *Mon. Wea. Rev.,* **137,** 2105–2125.

——, ——, J. F. Gamache, and F. D. Marks, 2011: Performance of convection-permitting hurricane initialization and prediction during 2008–2010 with ensemble data assimilation of inner-core airborne Doppler radar observations. *Geophys. Res. Lett.,* **38,** L15810, doi:10.1029/2011GL048469.

Zhang, J. A., R. F. Rogers, D. S. Nolan, and F. D. Marks Jr., 2011: On the characteristic height scales of the hurricane boundary layer. *Mon. Wea. Rev.,* **139,** 2523–2535.

Zhao, Q., and Y. Jin, 2008: High-resolution radar data assimilation for Hurricane Isabel (2003) at landfall. *Bull. Amer. Meteor. Soc.,* **89,** 1355–1372.